Journal of Microscopy, Vol. 234, Pt 1 2009, pp. 38–46
Received 4 October 2008; accepted 7 November 2008

TIRF microscopy evanescent field calibration using tilted fluorescent microtubules

C. GELL*,‡, M. BERNDT*,‡, J. ENDERLEIN† & S. DIEZ*
*Max-Planck-Institute of Molecular Cell Biology and Genetics, Dresden, Germany
†III. Institute of Physics, Georg-August-University, Göttingen, Germany

Key words. Evanescent field, microscope calibration, microtubules, penetration depth, TIRF.

Summary

Total internal reflection fluorescence microscopy has become a powerful tool to study the dynamics of sub-cellular structures and single molecules near substrate surfaces. However, the penetration depth of the evanescent field, that is, the distance at which the excitation intensity has exponentially decayed to 1/e, is often left undetermined. This presents a limit on the spatial information about the imaged structures. Here, we present a novel method to quantitatively characterize the illumination in total internal reflection fluorescence microscopy using tilted, fluorescently labelled, microtubules. We find that the evanescent field is well described by a single exponential function, with a penetration depth close to theoretically predicted values. The use of *in vitro* reconstituted microtubules as nanoscale probes results in a minimal perturbation of the evanescent field; excitation light scattering is eliminated and the refractive index of the sample environment is unchanged. The presented method has the potential to provide a generic tool for *in situ* calibration of the evanescent field.

Introduction

Total internal reflection fluorescence (TIRF) microscopy has emerged as a powerful tool to study a wide range of biological systems (Thompson & Steele, 2007). Because of the relative ease of installation on conventional inverted microscopes in a through-the-objective configuration (Axelrod *et al.*, 1984; Conibear & Bagshaw, 2000; Gell *et al.*, 2006), it has now become commonplace both in the study of live cells (Mashanov *et al.*, 2004; Manneville, 2006) and a variety of *in vitro* reconstituted biological assays at the single molecule level (Gell *et al.*, 2006). The technique is typically used only to provide fluorescence excitation in a thin, imprecisely quantified, sub-wavelength layer near the sample substrate. Indeed for many applications, the exact profile and penetration depth is unimportant. However, with the increasing application of TIRF as a routine laboratory tool, it will become of use to have a method to ensure reproducible penetration depths in different experiments as well as similar penetration depths at different excitation wavelengths.

In addition, the strong z-axis dependence of the excitation intensity in TIRF microscopy makes it potentially of use in obtaining sub-wavelength resolution quantitative data regarding molecular motion in z. Almers and co-workers used a calibrated evanescent field to monitor the axial motion of single secretary granules in live cells (Steyer & Almers, 1999). Very recently, a calibrated evanescent field has been used to perform high-resolution axial measurements of complexes on the plasma membrane of living cells (Saffarian & Kirchhausen, 2008).

The evanescent field generated upon total internal reflection of a laser beam at the interface between a substrate (typically glass) and a sample (typically an aqueous solution) has been described theoretically (Axelrod *et al.*, 1984). It follows that the expected intensity profile in z (perpendicular to the interface) is given by

$$I_{\mathrm{ex}}(z) = I_0 \exp(-z/d), \tag{1}$$

where I_0 is the evanescent field intensity at the interface and d is the characteristic penetration depth of the field, given by

$$d = \frac{\lambda}{4\pi\sqrt{n_1^2 \sin^2\theta - n_2^2}}, \tag{2}$$

where λ is the wavelength of the light used, n_1 and n_2 the refractive indices of the substrate and the sample, respectively ($n_1 > n_2$), and θ is the angle of incidence of the laser beam to the interface, some value above the critical angle (θ_c) for total internal reflection, given by

$$\theta_C = \sin^{-1}(n_2/n_1). \tag{3}$$

‡These authors contributed equally to this work.

Correspondence to: S. Diez. Tel: +49-351-210-2521; fax: +49-351-210-2020; e-mail: diez@mpi-cbg.de

Thus, the evanescent field exponentially decays in intensity into the lower refractive index medium with a penetration depth that depends, for a given interface, only on the laser beam angle of incidence (AOI) and the wavelength of light. The penetration depth is therefore independent of the polarization of the light used; however, the polarization of the incident laser light does affect both the intensity and polarization of the evanescent field (Axelrod *et al.*, 1984). It should be emphasized that, as shown by Eq. 1, the penetration depth does not represent an absolute limit on the depth of features in a sample that will be observed. Rather the penetration depth is the distance over which the intensity of the evanescent field drops to about 37% (corresponding to 1/e) of the value at the surface.

Several examples of methods to determine the penetration depth or to characterize fully the evanescent field profile exist in the literature: Steyer & Almers (1999) used fluorescent beads that were non-specifically adsorbed to the surface of a lens resting on a cover glass. Images of the beads using TIR excitation and also the more uniform excitation light provided by an arc-lamp (EPI-fluorescence mode) allowed the authors to produce an intensity versus height profile for a single laser AOI that could be described by a single exponential function. Similarly, the authors were able to produce a calibration curve for the evanescent field in conditions closer to their *in vivo* studies using beads randomly attached to the top surfaces of PC-12 cells and to the cover glass substrate between adsorbed cells. Mattheyses & Axelrod (2006) imaged fluorescently labelled 8.85-μm-diameter spheres resting on a cover glass surface. The assumed geometry at the sphere–glass interface allowed the reconstruction of the z profile of the excitation from x–y plane fluorescence images. The authors employed low refractive index ($n = 1.42$) spheres bathed in an index matching solution to prevent excitation light scattering (importantly in an effort to leave the evanescent field unperturbed). The authors were able to probe several different angles of incidence of the exciting laser beam and the results showed, interestingly, double-exponential curves where the major amplitude component (90%) had a decay length consistent with the theoretically derived penetration depth. The lower-amplitude component was assigned to far field excitation propagating into the solution due to scattering and reflections. Sarkar *et al.* (2004) employed a fluorescent atomic force microscope tip, which could be moved with nanometre precision vertically through the evanescent field, in order to completely characterize the profile. They obtained single exponential intensity profiles in z with penetration depths in good agreement with the theory. However, in that study, the absolute laser beam angles of incidence were not measured. Finally, Harlepp *et al.* (2004) combined TIRF excitation and fluorescence correlation spectroscopy. They were able to fit autocorrelation curves of the fluorescence intensity fluctuations from dye molecules diffusing in the evanescent field with an analytical model assuming single exponential character. They showed penetration depths consistent with the theory, although their method leaves the intensity profile of the evanescent field uncharacterized.

In this study, we present a novel method to quantitatively characterize the illumination in TIRF microscopy that requires no special analysis techniques, instrumentation or index matching. We immobilize *in vitro* reconstituted fluorescently labelled microtubules in a low-concentration agarose gel such that one end touches, or is near, the cover glass surface with the long axis of the microtubule at some degree of tilt to the surface (Fig. 1). Microtubules are filamentous structures composed of the globular protein tubulin that polymerizes into protofilaments arranged into hollow tubular structures (Alberts *et al.*, 2002). Microtubules are approximately 25 nm in diameter consisting of, typically, 13 or 14 laterally aligned protofilaments and are straight and rigid (a persistence length of up to 5 mm [Gittes *et al.*, 1993]) with a typical length of up to several tens of micrometres. Although microtubules form a large part of the cellular scaffold (the cytoskeleton) found in eukaryotes and play roles in cell division, as well as organelle transport, they can easily be reconstituted *in vitro* using standard protocols (Howard & Hyman, 1993).

Fluorescence images of the microtubules are acquired on an inverted microscope with the focus placed at the cover glass surface. Images for TIRF (Fig. 1(A)) or conventional arc-lamp excitation epi-fluorescence (EPI, Fig. 1(C)) illumination are shown in Figs 1(B) and (D), respectively. The TIRF image intrinsically contains z-axis information about the profile of the illuminating light due to the microtubule tilt: different parts along the long axis of the microtubule experience different excitation intensities and so map the vertical profile of the excitation light. The image of the same microtubule in EPI mode (Fig. 1(D)) reveals the comparatively weak decay of the detected fluorescence intensity along the microtubule, which for EPI illumination is only due to the inability to collect light efficiently from all points of the microtubule at the same time. Together with the determination of the microtubule tilt angle (see Equipment and Methods), the acquisition of one TIRF and one EPI image per microtubule allows us to directly obtain the evanescent field profile for a given AOI.

We show that for a correctly aligned TIRF microscope, imaging into an aqueous solution, the evanescent field is well described by a single exponential function in agreement with the theory above. Furthermore, we show that when tuned to short penetration depths – using AOIs far beyond the critical angle for total internal reflection (TIR) – the penetration depth is reliably described by Eq. 2 and is in the range from 80 to 100 nm. However, near the critical angle for TIR, Eq. 2 is less useful as errors in the refractive indices of the oil–cover glass–sample used, along with difficulties in accurately setting the laser AOI, make calculations unreliable. This reinforces the usefulness of an *in situ* calibration method, especially where deep penetration depths are desired.

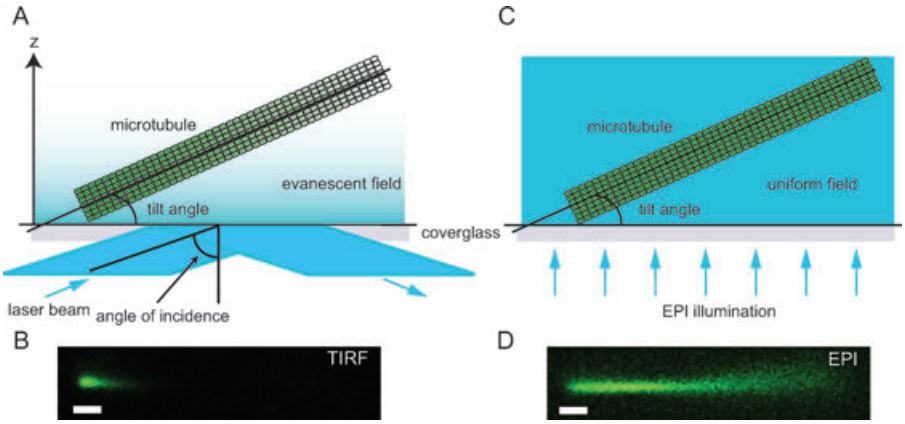

Fig. 1. Schematic of the experimental geometries (not to scale). A microtubule, fluorescently labelled with Alexa Fluor 488, is immobilized at some tilt angle (with respect to the cover glass surface) in a low agarose content gel (not shown). (A) An evanescent field, decaying exponentially away from the glass surface is generated by a laser beam incident above the critical angle for TIR. The evanescent field excites fluorescence with an intensity that varies along the long axis of the microtubule. Regions of the microtubule further from the glass surface experience less excitation intensity and so show lower fluorescence emission intensity. (B) x–y plane TIRF-image of the tilted microtubule depicted in A. (C) The same microtubule is recorded in EPI-mode, where all points along the microtubules are illuminated with uniform excitation intensity. (D) x–y plane EPI-image of the tilted microtubule depicted in C. Scale bars in B and D are 1 μm (x–y).

Equipment and methods

Microtubule preparation

Microtubules labelled with Alexa Fluor 488 were polymerized from a mixture of labelled and unlabelled porcine brain tubulin (4 mg mL^{-1}, 1 : 3 labelled : unlabelled tubulin) in BRB80 buffer (80 mM PIPES, 1 mM EGTA, 1 mM $MgCl_2$, pH 6.9) supplemented by 1 mM additional $MgCl_2$ and 1 mM GMPCPP at a final volume of 50 μL. After incubation for 2 h at 37°C, the polymerized microtubules were additionally stabilized by diluting into BRB80 containing 10 μM Taxol (BRB80T), to a final volume of 500 μL. The solution was centrifuged for 5 min at 134 000×g. The resulting pellet was re-suspended in 50 μL of BRB80T.

Microtubule immobilization

Five to 10 μL of the microtubule solution (varied to adjust the final density of microtubules immobilized in the gel) was added to an agarose anti-fade solution made in the following way: 10 μL of an anti-fade solution (6.9 μL BRB80T, 176 mM D-glucose, 0.070 mg mL^{-1} catalase, 0.176 mg mL^{-1} glucose-oxidase, 4.3% BME) was added to 40 μL of a 1% agarose solution (in BRB80 buffer). Both solutions were kept at a temperature of 37°C to prevent agarose polymerization during mixing. Ten microlitres of this mixture was then placed on a microscope slide and covered with a cover glass (Corning, zinc-titania glass $n = 1.523$ @ 589 nm); both glasses were preheated to 37°C. A thin (approximately 20 mm × 2 mm) piece of stretched Parafilm was placed on one side of the slide–cover glass sandwich before bringing them together; this prevents the two glasses pressing together too intimately that tended to result in microtubules flat on the glass surfaces. The slide-sandwiched solution was then removed from the heater and allowed to reach room temperature to allow the agarose gel to solidify.

Optical imaging

An inverted microscope (Zeiss Axiovert 200M, Zeiss, Oberkochen, Germany) was used in combination with a 100× apochromat TIRF-objective (NA 1.46, Zeiss) and EMCCD camera (Andor iXon, Belfast, N. Ireland). For TIRF illumination, a laser (Cobolt Calypso 50, $\lambda = 491$ nm) was coupled into an optical fibre, which then fed the light into a custom-made TIRF condenser where it was focused onto the back-focal plane of the objective. The lateral distance of the focus from the back-focal point could be varied using a differential micrometre that translated the fibre in the TIRF condenser. This allowed the AOI of the laser beam emerging from the objective at the substrate to be adjusted. The laser power was set to 50 μW, measured after the sample and with the laser beam pointing straight through the objective (AOI of 0°). The filters used to excite and TIRF-image the Alexa Fluor 488 labelled microtubules were excitation Z491/591X, dichroic mirror Z491/591DIC, emission ET525/50M (all filters from Chroma, Rockingham, VT, USA; our system is capable of dual colour operation; however, for this study only blue excitation and green emission were used). For EPI-fluorescence imaging, a fibre-coupled arc lamp and FITC filter combination were used (excitation D488/10, dichroic Z488RDC, emission ET525/50M). Data were recorded with an additional tube lens (1.6×) inserted giving a 100 nm x–y pixel resolution.

In every sample tilted microtubules had to be located and identified. This search was carried out in EPI-mode with reduced illumination power to avoid photobleaching. A microtubule was then imaged in TIRF at six different AOI (two images per angle, exposure time 400 ms each, averaged). Subsequently, a z stack of the microtubule was recorded in EPI mode (50 nm step size, typically over 10 μm total height to capture the entire microtubule) to determine the tilt angle and obtain the EPI correction image (see Results).

Determination of microtubule tilt angle

From the recorded EPI z stack three maximum projections of the microtubule in three orthogonal directions (projections in the z, x and y directions) were produced (see Supplementary Material). From these three projections, the microtubule tilt angle can be calculated with respect to the cover glass surface after correcting for axial aberration (Hell *et al.*, 1993) due to imaging in an aqueous environment with an oil-immersion TIRF objective (see Supplementary Material).

Determination of laser AOI

The AOI was set by adjustment of a micrometre that positions the laser focus in the TIRF objective's back-focal plane. In order to calibrate the micrometre to particular AOIs, an isosceles triangular prism (Thorlabs, Newton, NJ, USA, BK7 glass) was mounted on the sample stage. The geometry of the prism prevents TIR at AOIs where it would normally occur for a flat cover glass. The transmitted beam could then be observed on a screen mounted several metres to one side of the microscope. Taking the geometry of the prism into account, the distance to the screen and the height of the beam on the screen, it is possible to calculate the AOI of the laser beam at the first prism surface using Snell's law and basic trigonometry. The angular range for the AOIs chosen here covered almost the entire range of possible TIRF angles: from 63.2°, near the critical angle (approximately 61.6°), to 72.2°, the angle shortly before the TIRF image vanishes (due to the finite back aperture–numerical aperture of the objective). Errors in determining the TIRF angle were mainly caused by uncertainties of the position of the laser spot on the screen and determined to be between ±0.3° and ±0.4° depending on the AOI.

Determination of refractive indices

To allow *a priori* calculation of the penetration depth versus AOI behaviour (Eq. 2), the refractive indices of the cover glass and solution were determined to be $n_1 = 1.5156$ and $n_2 = 1.3393$, respectively. The value for the refractive index of the cover glass was assumed to be equal to the refractive index of the immersion oil we used (Zeiss Immersol 518F, Zeiss). The refractive index values for the immersion oil and the agarose–anti-fade–microtubule solution used in all experiments were determined using a refractometer (AR4D, Krüss, Hamburg, Germany) with illumination light in the range 483–493 nm.

Results

TIRF images of the same fluorescent dye-labelled microtubule immobilized in an agarose gel and tilted at 11.6° ± 0.1° to the cover glass substrate are shown in Fig. 2(A) at six different laser AOIs. In these x–y images, the objective's focus is placed near the cover glass surface, and the part of the microtubule on the left of each image is closest to the cover glass. One can immediately observe the rapidly decaying intensity profile in the fluorescence as one moves axially along the microtubule (left to right; direction in which the height of the microtubule above cover glass substrate increases). Similarly, it is immediately apparent that as the

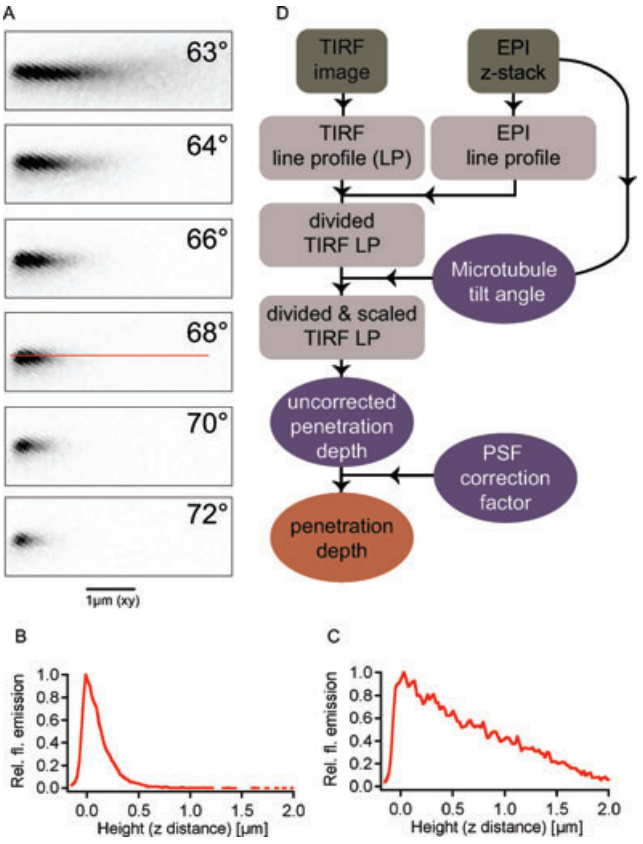

Fig. 2. Determination of penetration depths from TIRF and EPI intensity profiles along microtubule images. (A) TIRF images of a fluorescent microtubule with a 11.6° ± 0.1° tilt angle at six AOIs between approximately 63° and approximately 72° (top to bottom). (B) Intensity profile (red) from the 68° laser AOI image shown in A (red line in image). The abscissa of the intensity profile is rescaled to z using the measured tilt angle. (C) Intensity profile as in B and of the same microtubule but with EPI illumination. (D) Flowchart illustrating the process of data collection, analysis and correction. Dark and light grey boxes represent raw and processed data, respectively. Ellipses represent numerical values.

AOI is increased, the expected (Eq. 2) concomitant shorting of the penetration depth is observed.

Because the microtubule is straight, the observed intensity profiles along the microtubule's length accurately reflect the variation of detected emitted light with object height. Shown in Fig. 2(B) is the intensity profile (red) for the 68° AOI image shown in Fig. 2(A) (red line). The orientation of the abscissa of the intensity profile is chosen parallel to the microtubule in the image and is re-scaled to the effective z height sampled by the microtubule using the measured tilt angle (see Equipment and Methods, simply $z = x\tan(\theta_{\text{tilt}})$, with $\theta_{\text{tilt}} = 11.6^\circ \pm 0.1^\circ$; also see Fig. 1). The effect of this gently tilted microtubule is that its z height above the surface increases gradually along its length, and so the rapidly decaying evanescent field (in z) is spread over a much longer distance (in x–y). For this example, the tilt angle results in an effective sub-wavelength z resolution of approximately 20 nm per x–y pixel, meaning that an accurate profile of the evanescent field can be determined. The rapid decay of the intensity profile due to TIR excitation is in striking contrast to the intensity profile from the EPI-illumination (pseudo-uniform illumination, see Supplementary Information) image of the same microtubule (Fig. 2(C)). Note that as a typical Gaussian profile laser beam is used to generate the evanescent field, stronger intensity illumination is commonly seen in the centre of images compared with the periphery. In our microscope, this variation did not appear to be significant over the length of imaged microtubules (as we determined from the intensity profile along flat microtubules). Nevertheless, the magnitude of this effect might vary in different microscopes and so should be considered, especially when deep penetration depths are determined from microtubules with shallow tilt angles.

To investigate the exact profile of the excitation light, it is essential to account for the convolution of the object with the three-dimensional point spread function (PSF). Although the PSF is assumed to be translationally invariant perpendicular to the optical axis, that is, in the x–y plane, it varies in the z direction due to an effective reduction of the TIRF objective's numerical aperture with increasing object height and decreased near-field coupling of the emission light into the glass (Enderlein & Böhmer, 2003). We describe the measured fluorescence intensity I_C of an object (image coordinate space; x, y, z) by the convolution of the illuminated object (object coordinate space; x_0, y_0, z_0) with the PSF of the imaging system:

$$I_C(x,y,z) = \int_0^\infty \int_{-\infty}^{\infty} \int_{-\infty}^{\infty} I_{\text{ex}}(x_0,y_0,z_0)\cdot F(x_0,y_0,z_0) \times PSF(x-x_0,y-y_0,z-z_0)\,dx_0\,dy_0\,dz_0, \tag{4}$$

where I_{ex} describes the illumination (excitation) profile and F is the fluorescent object function describing the distribution of fluorescent molecules in the object. Taking into account the specific geometry of the object – a tilted microtubule chosen to be parallel to the x axis – we can write the expression for the intensity dependence of the intensity profiles obtained from the TIR and EPI images as (see Supplementary Information):

$$I_C^{\text{TIR}}(x) \propto \int_0^{L\cdot\cos\theta_{\text{tilt}}} I_{\text{ex}}^{\text{TIR}}(x_0\tan\theta_{\text{tilt}})\cdot F\left(\frac{x_0}{\cos\theta_{\text{tilt}}}\right) \times PSF(x-x_0,0,-x_0\tan\theta_{\text{tilt}})\,dx_0, \tag{5}$$

$$I_C^{\text{EPI}}(x) \propto \int_0^{L\cdot\cos\theta_{\text{tilt}}} F\left(\frac{x_0}{\cos\theta_{\text{tilt}}}\right) \times PSF(x-x_0,0,-x_0\tan\theta_{\text{tilt}})\,dx_0, \tag{6}$$

where $I_{\text{ex}}^{\text{TIR}}$ describes the non-uniform TIR illumination in z.

Comparison of Eqs 5 and 6 shows that one could derive the TIR excitation profile by simply dividing the two equations if the influence of the PSF were negligible, that is, if the PSF could be described by a Dirac delta function in x_0. (In fact as we will show later on this strategy is reasonable for shallow microtubule tilt angles.) However, due to the finite width of the PSF an additional correction is necessary. This can be understood in the following way: Every point in the microtubule image is influenced by every part of the microtubule. Although in the case of EPI illumination all parts contribute with similar intensity, they contribute with different amounts in TIR, where the illumination is highly non-uniform on the length scale of the PSF.

Data processing for both TIRF and EPI images proceeds in the following manner (see Fig. 2(D) and Supplementary Information for additional detail): First a background subtraction by averaging areas surrounding the microtubule is performed (all analysis is carried out in software written for this task in Igor Pro 6, Wavemetrics, Portland, OR, USA). To account for the lateral blur in the image, the intensity perpendicular to the microtubule for five pixels either side of the microtubule centre line is integrated. Although the line width can be arbitrary (and just needs to be the same in the EPI and the TIRF image), it is advisable to integrate over a width of at least twice that of the PSF in order to account for the blurring effects. This results in 1D intensity profiles of the measured signal along the projected image of the microtubule (corresponding to Eqs 5 and 6). The TIRF intensity profile is then divided by the similarly processed EPI intensity profile, which has itself been normalized (to unity). These line profiles (resulting from the TIRF images in Fig. 2(A)) are presented in Fig. 3(A) (red lines), for each AOI measured. The abscissa is rescaled to z based on the microtubule tilt angle (here $11.6^\circ \pm 0.1^\circ$). We find that the line profiles at all AOIs are well described by single exponential functions (black lines) with decay lengths in the range 80–1100 nm.

In order to determine the correction factor due to the finite-width PSF numerical simulations of the experiment were performed. It is assumed that the microtubule is homogeneously labelled with fluorescent dye molecules

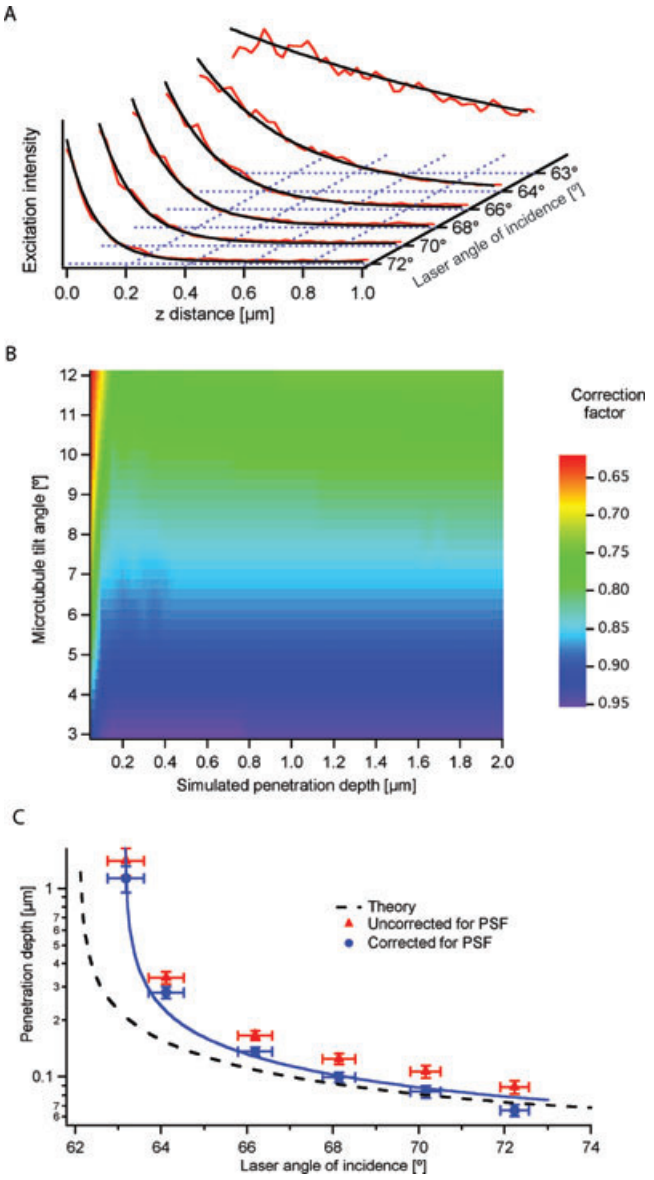

Fig. 3. Determination of the corrected penetration depths. (A) Line profiles along the microtubules in the images shown in Fig. 2(A) that have been divided by the EPI intensity profile of the same microtubule. The abscissa has been scaled to the equivalent *z* distance, based on the microtubule tilt angle. Each curve is well described by a single exponential function (black). (B) Simulations allow estimation of the effect of the finite PSF. This 3D plot shows the magnitude (colour) of the multiplicative correction factor needed (colour scale; blue – less correction, red – more correction). (C) The experimentally determined mean penetration depth versus AOI for six different microtubules with tilt angles ranging from 3.5° to 11.6°. Shown are both the PSF-uncorrected and PSF-corrected penetration depths (red triangles and blue circles, respectively). Error bars on the ordinate are the standard error of the mean and error bars on the abscissa are estimates of the error in the determination of the AOI. The expected theoretical relationship (Eq. 2) is shown as a dashed line, using experimentally derived estimates for the refractive indices of the glass and solution. The data are, however, best described by a fit of Eq. 2 with refractive indices as free parameters (blue line).

having isotropically distributed orientations. The microtubule tilt angle defines the position of a line of emitters in the simulated object volume and the excitation intensity at that height (either TIR or EPI) modulates the strength of their emission. The projected images that would be produced by these emitters at the camera are then computed numerically evaluating the integrals in Eqs 5 and 6 above. The PSF is calculated following Enderlein & Böhmer (2003): The angular distribution of emission on the cover glass surface (the plane of focus, $z_0 = 0$) for an electric dipole emitter at a position ($x_0 = 0$, $y_0 = 0$, z_0) is first derived. This distribution is used for calculating the energy flux of the electromagnetic field on the CCD as a function of position (x, y, $z = 0$), using the general ideas of Richards and Wolf (1959; Wolf, 1959) concerning light focusing and imaging through optics with high numerical aperture (see also Török *et al.*, 1998; Higdon *et al.*, 1999; Török, 2000; Enderlein & Böhmer, 2003). Then the fluorescence intensities in the simulated TIRF and EPI images are integrated perpendicular to the microtubule orientation, resulting in a fluorescence intensity profile as a function of position along the microtubule. The intensity profile under TIRF illumination is divided by the profile under EPI, and the curves are scaled to *z*. This process therefore precisely follows the experimental method. All calculations were done for an excitation wavelength of 491 nm and a centre emission wavelength of 525 nm. The refractive index of water was set to 1.33, that of glass to 1.52. The imaging objective had a numerical aperture of 1.46, the imaging magnification was set to a value so that one image pixel corresponded to a square of 100 × 100 nm^2 in sample space. The simulations were then repeated for a range of microtubule tilt angles as a function of penetration depth of the exciting TIR evanescent field. Each of these simulated line profiles are well described by a single exponential function, allowing us to produce a plot of correction factors relating the simulated penetration depth with the true penetration depth of the evanescent field used to seed the simulation (Fig. 3(B)). For penetration depths larger than approximately 100 nm the variation of the correction factor with penetration depth is weak; however, at shorter penetration depths the correction factor varies more strongly, particularly for steeply tilted microtubules. By contrast, the correction factor varies significantly with microtubule tilt angle at all penetration depths but particularly so for short penetration depths (<100 nm). Nevertheless, it can be seen that for microtubules with shallow tilt angles (<4°), the correction factor is small (5–10%) and does not vary with penetration depth.

The simulations highlight several important aspects: (1) The line profiles resulting from division of the simulated TIRF intensity profiles with the simulated EPI intensity profiles are well described by single exponential functions. Thus, experimental line profiles that are well described by a single exponential function (as in fact is the case, see Fig. 3(A)) are consistent with the underlying TIRF illumination profiles

being single exponential. (2) The simulated penetration depths (corresponding to the uncorrected penetration depths in the experiments) over-estimate the true penetration depth by between 2 and 35%. (3) The degree of error is strongly dependent on the microtubule tilt angle but weakly dependent on the penetration depth, except at very short penetration depths.

We then experimentally determined the uncorrected penetration depths for six microtubules with tilt angles ranging from 3.5° to 11.6° at AOIs between 63° and 72°. These data are shown in Fig. 3(C) (red triangles) together with the corrected values (blue circles). The penetration depth versus AOI relationship follows the expected trend for both uncorrected and corrected penetration depths (Fig. 3(C) dashed black line, a plot of Eq. 2 with experimental estimates for $n_1 = 1.5156$ and $n_2 = 1.3393$, see Equipment and Methods). However, at lower AOIs, approaching the critical angle determined by these refractive indices, there is a strong discrepancy in the absolute values obtained. At higher AOIs, a smaller but significant systematic offset is seen for the uncorrected, but not for the corrected, penetration depths. In fact, the corrected penetration depths (but *not* the uncorrected ones) can be well described at all AOIs using modified estimates for n_1 and n_2 (Fig. 3(C) solid blue line, best fit of Eq. 2 to the corrected penetration depths with $n_1 = 1.51$ and $n_2 = 1.34$).

Discussion

We have shown how tilted fluorescent microtubules can be used as probes of the evanescent field generated by TIR illumination. Determination of the microtubule tilt angle allows the *z*-axis illumination profile to be accurately characterized using a standard *x*–*y* image.

The TIRF evanescent field excitation line profiles we have obtained here are well described by single exponential functions, consistent with the theory (Eq. 1). Another study, using spheres on the surface rather than microtubules, obtained curves best fit by double exponentials (Mattheyses & Axelrod, 2006). There the major amplitude had a decay length consistent with the expected penetration depth, whereas the low-amplitude component (approximately 10%) possessed a decay length that was assigned to scattered, propagating excitation light. In our study, we see no evidence of a propagating component – importantly our data are well fit both before *and* after PSF correction by a single exponential. This, in fact, reinforces the idea those authors presented: that these effects are somewhat equipment and application specific, highlighting the need for accurate and convenient *in situ* calibration techniques. Furthermore, the data presented by Mattheyses *et al.* are uncorrected both with respect to the PSF and the decreasing efficiency of light collection with increasing height above the plane of focus: In our study, using low scattering probes (microtubules) we were able to correct for variations in the height-dependent collection efficiency using uniform EPI excitation light. Presumably, this is more difficult with 3D macroscopic probes due to the influence of out of focus fluorescence and scattering. It should be noted that in experiments where the environment may be more heterogeneous and refractive (e.g. live cell imaging), stray and scattered light might lead to fluorescence from objects significantly deeper than the penetration depth.

Our data show that at large AOIs, the corrected TIRF penetration depths are in good agreement with theory using experimental estimates for the refractive indices of the solution and cover glass (cf. Fig. 3(C), blue circles with dashed line). However, agreement near the critical angle for TIR is less good. We suggest that this discrepancy is mainly due to errors in the estimates for the refractive indices. Equation 2, describing this relationship, is relatively insensitive to the refractive indices at AOIs far above the critical angle (i.e. at short penetration depths). By contrast, at low AOIs (i.e. long penetration depths), the precise refractive indices of the materials are crucial in predicting the penetration depth. As an illustration, our data are well described by a combination of refractive indices (Fig. 3(C) blue line, a fit of Eq. 2) that only differ by less than 0.1% to those we measured independently. This is significant because estimates for the refractive index of the materials used are often only available for one wavelength at one temperature and are difficult to measure.

As was discussed, the influence of the finite PSF is important. Simulations revealed that neglecting this effect leads to an overestimation of the true penetration depth by around 2–35%, depending on the microtubule tilt angle. The plot shown in Fig. 3(B) reveals that the correction factor is largely independent of penetration depth but strongly varies with microtubule tilt angle. This can be explained by the shape of the PSF: Its finite width averages the strong intensity variation along the microtubule under TIRF illumination. For a given point in the *x*–*y* plane of the image, the PSF averaging occurs over a larger range of intensities the steeper the microtubule is oriented. Hence, the tilt angle of the microtubule mainly determines the error made due to the finite width of the PSF, not the actual penetration depth itself.

Tilted microtubules might also be useful for calibration in TIRF-based single molecule fluorescence tracking experiments (Sarkar *et al.*, 2004; Saffarian & Kirchhausen, 2008). In particular, microtubule intensity profiles as in Fig. 2(B) incorporate all imaging effects and therefore directly give the collected fluorescence emission versus height dependence. Although PSF blur from adjacent parts of the microtubules is still present in these intensity profiles, our simulations suggest that for shallow tilt angles (<4°) and moderate penetration depths (>100 nm), the error is below 10%.

In conclusion, our results demonstrate the possibility to extract the precise experimental illumination profile in TIRF microscopy using tilted fluorescent microtubules. Moreover, our findings illustrate the importance of an *in situ* method to directly measure the true penetration depths and evanescent

field profiles – especially near the critical angle – for each TIRF microscope, individually. Our results show, for a well-aligned TIRF system imaging a sample in an aqueous environment, that the excitation light profile is single exponential. For AOIs far from the critical angle for TIR, the established theory (Eqs 1–3) can be used to reliably estimate the penetration depth. However, in cases where long penetration depths are needed, or where the quality of the alignment of a microscope is uncertain, *in situ* calibration is essential.

The simplicity of our method, compared with previous approaches, means that TIRF field calibration could be performed routinely. Because no index matching is required, the refractive index of the surrounding medium can easily be changed to mimic the conditions of the biological experiments being performed. Microtubules with a diameter of about 1/20 of the optical wavelength, a 1D macroscopic size of up to tens of micrometres and high rigidity make them perfect nanoscale probes. *In vitro* reconstitution and fluorescent labelling is straightforward, and indeed both tubulin and pre-polymerized fluorescent-labelled microtubules are becoming commercially available. In the future, microtubules may thus provide an interesting alternative to beads in microscope calibration and add to the general light-microscopy toolbox.

Acknowledgements

The authors thank Cécile Leduc for experimental help, Erik Schäffer, Gary Brouhard, Claire Friel, Manfred Lein and Jonathon Howard for helpful discussions and Marija Žanić for comments on the manuscript. This work was supported by the German Research Foundation (DFG SPP 1128), the Federal Ministry of Education and Research (03N8712) and the Max-Planck-Society.

References

Alberts, B., Johnson, A., Lewis, J., Raff, M., Roberts, K. & Walter, P. (2002) *Molecular Biology of the Cell*. Garland, New York, USA.

Axelrod, D., Burghardt, T.P. & Thompson, N.L. (1984) Total internal-reflection fluorescence. *Ann. Rev. Biophys. Bioeng.* **13**, 247–268.

Conibear, P.B. & Bagshaw, C.R. (2000) A comparison of optical geometries for combined flash photolysis and total internal reflection fluorescence microscopy. *J. Microsc.-Oxford* **200**, 218–229.

Enderlein, J. & Böhmer, M. (2003) Influence of interface-dipole interactions on the efficiency of fluorescence light collection near surfaces. *Opt. Lett.* **28**, 941–943.

Gell, C., Brockwell, D.J. & Smith, D.A.M. (2006) *Handbook of Single Molecule Fluorescence Spectroscopy*. Oxford University Press, Oxford, U.K.

Gittes, F., Mickey, B., Nettleton, J. & Howard, J. (1993) Flexural rigidity of microtubules and actin-filaments measured from thermal fluctuations in shape. *J. Cell Biol.* **120**, 923–934.

Harlepp, S., Robert, J., Darnton, N.C. & Chatenay, D. (2004) Subnanometric measurements of evanescent wave penetration depth using total internal reflection microscopy combined with fluorescent correlation spectroscopy. *Appl. Phys. Lett.* **85**, 3917–3919.

Hell, S., Reiner, G., Cremer, C. & Stelzer, E.H.K. (1993) Aberrations in confocal fluorescence microscopy induced by mismatches in refractive-index. *J. Microsc.-Oxford* **169**, 391–405.

Higdon, P.D., Török, P. & Wilson T. (1999) Imaging properties of high aperture multiphoton fluorescence scanning optical microscopes. *J. Microsc.* **194**, 127–141.

Howard, J. & Hyman, A.A. (1993) Preparation of marked microtubules for the assay of the polarity of microtubule-based motors by fluorescence microscopy. *Methods Cell Biol.* **39**, 105–113.

Manneville, J.B. (2006) Use of TIRF microscopy to visualize actin and microtubules in migrating cells. *Method Enzymol.* **406**, 520–532.

Mashanov, G.I., Tacon, D., Peckham, M. & Molloy, J.E. (2004) The spatial and temporal dynamics of pleckstrin homology domain binding at the plasma membrane measured by Imaging single molecules in live mouse myoblasts. *J. Biol. Chem.* **279**, 15274–15280.

Mattheyses, A.L. & Axelrod, D. (2006) Direct measurement of the evanescent field profile produced by objective-based total internal reflection fluorescence. *J. Biomed. Opt.* **11**, 0140061–0140067.

Richards, B. & Wolf, E. (1959) Electromagnetic diffraction in optical systems II. Structure of the image field in an aplanatic system. *Proc. Roy. Soc. London* **253**, 358–379.

Saffarian, S. & Kirchhausen, T. (2008) Differential evanescence nanometry: live-cell fluorescence measurements with 10-nm axial resolution on the plasma membrane. *Biophys. J.* **94**, 2333–2342.

Sarkar, A., Robertson, R.B. & Fernandez, J.M. (2004) Simultaneous atomic force microscope and fluorescence measurements of protein unfolding using a calibrated evanescent wave. *Proc. Natl. Acad. Sci. U.S.A.* **101**, 12882–12886.

Steyer, J.A. & Almers, W. (1999) Tracking single secretory granules in live chromaffin cells by evanescent-field fluorescence microscopy. *Biophys. J.* **76**, 2262–2271.

Thompson, N.L. & Steele, B.L. (2007) Total internal reflection with fluorescence correlation spectroscopy. *Nat. Protocols* **2**, 878.

Török, P. (2000) Propagation of electromagnetic dipole waves through dielectric interfaces. *Opt. Lett.* **25**, 1463–1465.

Török, P, Higdon, P.D. & Wilson, T. (1998) Theory for confocal and conventional microscopes imaging small dielectric scatterers. *J. Mod. Opt.* **45**, 1681–1698.

Wolf, E. (1959) Electromagnetic diffraction in optical systems I. An integral representation of the image field. *Proc. Roy. Soc. London* **253**, 349–357.

Supporting Information

Additional Supporting Information may be found in the online version of this article:

Fig. S1. The normalized intensity profile along a titled microtubule measured in TIRF for a laser AOI of 63°, before (red) and after (blue) multiple measurements at other AOIs. These data show that the reproducibility of the AOI is good and that over the time course of a typical measurement neither bleaching nor microtubule depolymerization are significant effects.

Fig. S2. Intensity profiles along a steeply tilted (approximately 15.9°) microtubule in both uniform illumination (a laser beam at 0° AOI) and with EPI illumination are nearly identical.

Fig. S3. Method to determine microtubule tilt angle: A *z* stack (50 nm resolution) of a tilted microtubule was recorded using EPI illumination. Maximum projections were then made in the three orthogonal directions; shown above are the **A)**: *z* projection, **B)**: *x* projection and **C)**: *y* projection. Recording the microtubule angle with respect to two orthogonal axes allows calculation of the 'apparent' tilt angle with respect to the cover glass. **D)** The microtubule's central axis is located by multiple Lorentzian fits along the microtubule (three such fits are shown for illustration, which are the line profiles and fits along the similarly coloured lines shown in C). **E)** The slope of a plot of the microtubule *z* position (Lorentzian peak tops) versus position along the microtubule (E shows the plot for the image in C) gives the tangent of the microtubule angle from that projection.

Appendix S1. Supplementary information

Please note: Wiley-Blackwell are not responsible for the content or functionality of any supporting materials supplied by the authors. Any queries (other than missing material) should be directed to the corresponding author for the article.